

Low-energy physics of the t - J model in $d = \infty$ using extremely correlated Fermi liquid theory: Cutoff second-order equations

B. Sriram Shastry

Physics Department, University of California, Santa Cruz, California 95064, USA

Edward Perepelitsky

*Centre de Physique Théorique, École Polytechnique, CNRS, Université Paris-Saclay, 91128 Palaiseau, France
and Collège de France, 11 place Marcelin Berthelot, 75005 Paris, France*

(Received 26 May 2016; revised manuscript received 11 July 2016; published 28 July 2016)

We present the results for the low-energy properties of the infinite-dimensional t - J model with $J = 0$, using $O(\lambda^2)$ equations of the extremely correlated Fermi liquid formalism. The parameter $\lambda \in [0, 1]$ is analogous to the inverse spin parameter $1/(2S)$ in quantum magnets. The present analytical scheme allows us to approach the physically most interesting regime near the Mott insulating state $n \lesssim 1$. It overcomes the limitation to low densities $n \lesssim 0.7$ of earlier calculations, by employing a variant of the skeleton graph expansion, and a high-frequency cutoff that is essential for maintaining the known high- T entropy. The resulting quasiparticle weight Z , the low ω, T self-energy, and the resistivity are reported. These are quite close at all densities to the exact numerical results of the $U = \infty$ Hubbard model, obtained using the dynamical mean field theory. The present calculation offers the advantage of generalizing to finite T rather easily, and allows the visualization of the loss of coherence of Fermi liquid quasiparticles by raising T . The present scheme is generalizable to finite dimensions and a nonvanishing J .

DOI: [10.1103/PhysRevB.94.045138](https://doi.org/10.1103/PhysRevB.94.045138)

I. INTRODUCTION

The fundamental importance of the t - J model for understanding the physics of correlated matter, including high- T_c superconductors, has been recognized for many years [1]. The t - J model is a prototype of extreme correlations, incorporating the physics of (Gutzwiller) projection to the subspace of single occupancy. The added superexchange J provides the mechanism for quantum antiferromagnetism at half-filling, and upon hole doping, for superconductivity via singlet pairing [1]. This viewpoint has attracted much attention in the community. It has led to many approximate methods of calculation being applied to the t - J model, in order to calculate experimentally measured variables. Despite intense effort in recent years, schemes for *controlled* calculations are rare since the model has well-known fundamental complexities that need to be overcome.

Motivated by this challenge, we have recently formulated the extremely correlated Fermi liquid (ECFL) theory [2,3] for tackling the t - J and related $U \rightarrow \infty$ type models. The ECFL theory deals with the t - J model by viewing it as a noncanonical Fermi problem, and proceeds via a nonlinear representation of Gutzwiller projected fermions in terms of canonical fermions. It is pedagogically useful to draw a parallel [3] to the Dyson-Maleev representation of spins [4] used in quantum magnets. In this representation [4], the spins are hard core bosons, and are nonlinearly expressed in terms of the canonical bosons, namely, the spin waves. The ECFL methodology developed to date consists of successive approximations in the expansion parameter $\lambda \in [0, 1]$, playing a role analogous to the inverse spin parameter $1/(2S)$ in quantum magnetism. This analogy is developed in [3], where parallels between the ECFL calculations and earlier calculations of the partition function and Green's functions of the spin problem are drawn. It is useful to note that the classical limit for spins $1/S \rightarrow 0$ corresponds

to the limit of free-fermion limit $\lambda \rightarrow 0$. Continuity in λ leads to a protection of the Fermi surface volume for the interacting theory, i.e., the Luttinger-Ward volume theorem is obeyed. Low-order expansions can be performed analytically for the most part, and therefore have all the usual advantages of analytic approaches, such as explicit formulas for variables of interest and also flexibility for different situations. Several recent applications of the ECFL theory, mentioned below, show promise in terms of reproducing the salient features of exact numerical solutions of strong coupling models, wherever available [5,6]. The theory has also had success in reconciling extensive data on angle-resolved photoemission (ARPES) line shapes [7], including subtle features such as the low-energy kinks, and has made testable predictions on the asymmetry of line shapes [8].

In order to understand better the nature as well as limitations of a low-order expansion in λ , we have tested the solution against two important strongly correlated problems where the numerical renormalization group and related ideas provide exact numerical results. In [5], the asymmetric Anderson impurity problem, solved by Wilsonian renormalization numerical group methods [9–12] was used as one of the benchmarking models. Second, in [6], the $d \rightarrow \infty$ Hubbard model at large U , solved numerically by the dynamical mean field theory (DMFT) method [13–39], was used as the benchmarking model. These benchmarking studies show that the ECFL approach is overall consistent with the exact solutions, with some caveats. There are indeed differences in detailed structures at higher energies [40]. However, the raw initial results seem both useful and reliable for obtaining the low-energy spectrum, and for a broad understanding of the occupied side of the spectral functions. We further found that the calculations are *very close* to the exact solutions, *provided we scale the frequencies* by the respective quasiparticle weights Z of the two theories.

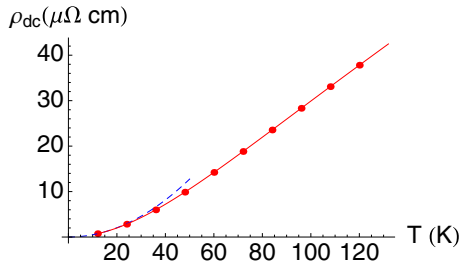


FIG. 1. ρ_{dc} on absolute scale vs T in Kelvin for particle density $n = 0.85$. We have used the estimates $D = 12000$ K and $\rho_0 = 258 \mu\Omega \text{ cm}$. The latter is obtained by using [57] $\rho_0 \approx \frac{h a_0 d}{e^2}$, where we estimate $a_0 d \approx 10^{-8}$ cm. The Fermi liquid behavior with quadratic resistivity in the blue dotted line breaks down above $T_{FL} \approx 30$ K, and is followed by a regime of linear resistivity.

The version of the ECFL presented in [6] and the closely related [5] is therefore promising, but has the limitation of being confined to low density $n \lesssim 0.7$. In the most interesting density range $n \lesssim 1$, it falls short of being a “standalone theory” since the magnitude of the calculated Z is too large. One requires rescaling frequencies to compensate for the incorrect magnitude of Z , and thereby improve the agreement. It is therefore important to find ways to extend this analytical approach to cover the physically most interesting density regime $0.7 \leq n \leq 1$. A diagnostic objective of this paper is to identify the cause for the inaccurate Z in the earlier version, and to explore ways to overcome it. We have found it possible to do both. This paper presents an alternative scheme that can be pushed to high-particle densities as well. We show here that the resulting scheme gives satisfactory results for most of the interesting low ω, T variables of the model.

Amongst the several variables of interest, the transport objects are the most difficult ones to compute reliably. The difficulty lies in their great sensitivity to the *lowest excitation energies*, and in the paucity of reliable tools to capture these. The limit of large dimensionality is helpful here since it has the great advantage of killing the vertex corrections [41]. Thus, a knowledge of the one-electron Green’s function can give us *the exact resistivity of a metal*, arising from inelastic mutual collisions of electrons. Despite the stated simplification, this calculation remains technically challenging. In important recent work, this calculation has been performed in [42,43] for the large- U Hubbard model in infinite dimensions. The authors have produced exact resistivity results that are so rare in condensed matter systems. We can use them to benchmark our results for the resistivity at different densities and temperature. We report the results of this comparison in this paper. Figure 1 shows one of the main results of the calculation presented here, the details leading to it are described below.

In Sec. II, we summarize the second-order equations and introduce the various Green’s functions and self-energies needed. In Sec. III, we identify the conditions necessary for getting a satisfactory Z near half-filling. In Sec. IV, after summarizing the self-consistency loop, we give a prescription for modifying the earlier equations and give the new set. This requires using a slightly different skeleton graph expansion, where certain objects are evaluated exactly using the number sum rule. The ECFL theory has some intrinsic freedom in

choosing the details of the skeleton expansion, more so than in the standard Feynman graph based canonical models. That freedom can be usefully employed here. We find that it is also obligatory to introduce a high-energy cutoff, in order to recover the known high- T entropy of the model. While the precise form of the cutoff is not uniquely given by theory, we found that several reasonable functional forms gave comparable results at low energies and low T , provided that the parameters were chosen to yield the *high- T* entropy. This cutoff also eliminates weak tails in the spectral functions that otherwise extend to large negative (i.e., occupied) energies.

In Sec. V, we present results for the T and n variation of the chemical potential and the quasiparticle weight Z . We also present the ω , T , and n variation of the self-energy and spectral functions, where the quasiparticles, the asymmetry of the spectral functions, and the thermal destruction of the quasiparticles are highlighted. In Sec. VI, we present results for the resistivity at low and intermediate T for various densities. In Sec. VII, we provide a summary and discuss the prospects for further work.

II. SUMMARY OF SECOND-ORDER ECFL THEORY

Let us begin by recounting the exact formal expression for the Green’s function of the t - J model. In the ECFL theory, this object is given exactly as

$$\mathcal{G}(k, i\omega_n) = \mathbf{g}(k, i\omega_n) \times \tilde{\mu}(k, i\omega_n), \quad (1)$$

a product of the auxiliary Green’s function \mathbf{g} and the “comparison” function [44] given in terms of a second self-energy $\Psi(k, i\omega_n)$ and the particle density n as $\tilde{\mu}(k, i\omega_n) = \{1 - n/2 + \Psi(k, i\omega_n)\}$. The auxiliary Green’s function $\mathbf{g}(k, i\omega_n)$ given by

$$\mathbf{g}(k, i\omega_n) = \frac{1}{i\omega_n + \mu - \{1 - n/2\} \varepsilon_k - \Phi(k, i\omega_n)}, \quad (2)$$

where μ is the chemical potential and ε_k the band energy. In the infinite-dimensional limit, it is demonstrated in [45] that an exact simplification occurs with these equations, whereby the momentum dependence is given by

$$\Psi(k, i\omega_n) = \Psi(i\omega_n), \quad (3)$$

$$\Phi(k, i\omega_n) = \chi(i\omega_n) + \varepsilon_k \Psi(i\omega_n), \quad (4)$$

where both Ψ and χ are functions of only the fermionic Matsubara frequency $\omega_n = (2n + 1)\pi\beta$, *but not the momentum k* . These expressions can be used in Eq. (1) and upon using the analytic continuation $i\omega_n \rightarrow \omega + i0^+$, we may express the Green’s function in the standard Dyson representation

$$\mathcal{G}(k, \omega + i0^+) = \frac{1}{\omega + i0^+ + \mu - \varepsilon_k - \Sigma(\omega + i0^+)}, \quad (5)$$

where the Dyson self-energy is now manifestly momentum independent, and given by

$$\Sigma(\omega + i0^+) = \mu + \omega + \frac{\chi(\omega + i0^+) - \mu - \omega}{1 - \frac{n}{2} + \Psi(\omega + i0^+)}. \quad (6)$$

This result demonstrates the momentum independence of the Dyson self-energy of the t - J model in infinite dimensions. It

is consistent with the analogous result for the Hubbard model at any U [13–15].

Within the ECFL theory we rely upon a systematic λ expansion to compute the two self-energies Ψ and χ . This λ expansion is described in detail in [2,46,47], in brief the parameter λ lives in the range $\in \{0,1\}$, and plays the role of the quantum parameter $1/(2S)$ in the large spin expansions familiar in the theory of magnetism. A skeleton diagram method can be devised for expanding the self-energies Ψ and χ in a formal power series in λ , with terms that are functionals of \mathbf{g} and the band energies ε_k . This expansion uses the full \mathbf{g} (rather than noninteracting propagators \mathbf{g}_0) as fundamental units, or “atoms,” for the expansion. The procedure is in close analogy with the skeleton diagram methods used in many-body theory. Having the self-energies to a given order in λ , one now reconstructs the Green’s functions self-consistently, the scheme is to second order in the present case.

The explicit equations to second order are found to be

$$\mathcal{G}(k, i\omega_n) = \mathbf{g}(k, i\omega_n) \{a_G + \lambda \Psi(k, i\omega_n)\}, \quad (7)$$

$$\begin{aligned} \mathbf{g}^{-1}(k, i\omega_n) &= i\omega_n + \boldsymbol{\mu}' - \lambda \chi(k, i\omega_n) \\ &\quad - \{a_G + \lambda \Psi(k, i\omega_n)\} \left(\varepsilon_k - \frac{u_0}{2} \right), \end{aligned} \quad (8)$$

with

$$a_G = 1 - \lambda \mathcal{G}(j, j^-) = 1 - \lambda \sum_k \mathcal{G}(k, i\omega_n) e^{i\omega_n 0^+}, \quad (9)$$

where $\boldsymbol{\mu}' = \boldsymbol{\mu} - \frac{u_0}{2}$. In Eq. (9), the middle (last) term is in space-time (wave-vector-frequency) variables, denoted respectively in the compact notation $j \equiv (\vec{R}_j, \tau_j)$, $k \equiv (\vec{k}, i\omega_n)$, and denoting $j^- \equiv (\vec{R}_j, \tau_j + i0^-)$. The two self-energy functions Ψ and χ are expanded formally in λ as $\Psi = \Psi_{[0]} + \lambda \Psi_{[1]} + \dots$ and $\chi = \chi_{[0]} + \lambda \chi_{[1]} + \dots$. A systematic expansion in λ is available to third order in [46], from the low-order results [48] we find $\Psi_{[0]} = 0, \chi_{[0]} = -\sum_p \mathbf{g}(p)(\varepsilon_p - \frac{u_0}{2})$ and

$$\Psi_{[1]}(k) = -\sum_{pq} (\varepsilon_p + \varepsilon_q - u_0) \mathbf{g}(p) \mathbf{g}(q) \mathbf{g}(p+q-k), \quad (10)$$

$$\begin{aligned} \chi_{[1]}(k) &= -\sum_{pq} \left(\varepsilon_{p+q-k} - \frac{u_0}{2} \right) (\varepsilon_p + \varepsilon_q - u_0) \\ &\quad \times \mathbf{g}(p) \mathbf{g}(q) \mathbf{g}(p+q-k). \end{aligned} \quad (11)$$

In view of the explicit factors of λ in Eqs. (7) and (8), this leads to an $O(\lambda^2)$ approximation for \mathcal{G} ; the recipe further requires that the parameter λ is set to unity before computing. Here, u_0 denotes the second chemical potential. It enters the theory as a Hubbard-type term with a self-consistently determined coefficient u_0 , as described in [47]. This chemical potential is essential in order to satisfy the shift invariance of the t - J model order by order in λ , namely, $t_{ij} \rightarrow t_{ij} + c \delta_{ij}$ with an arbitrary constant c . For instance, we see in Eq. (11) that a shift of the energies $\varepsilon_k \rightarrow c + \varepsilon_k$ is rendered immaterial due to the structure of the terms, the constant c can be absorbed into u_0 . The two chemical potentials $\boldsymbol{\mu}$ and u_0 are determined through the pair of sum rules on the auxiliary \mathbf{g} and the standard number

sum rule on \mathcal{G} :

$$\sum_k \mathbf{g}(k) e^{i\omega_n 0^+} = \frac{n}{2} = \sum_k \mathcal{G}(k) e^{i\omega_n 0^+}. \quad (12)$$

In dealing with Eq. (9), the composite nature of the \mathcal{G} in view in Eq. (1) offers a choice for implementing the skeleton expansion. Such a choice is absent in the more standard many-body problems. On the one hand, we could use the sum rule Eq. (12) for \mathcal{G} giving

$$a_G^{(I)} \rightarrow 1 - \lambda \frac{n}{2}, \quad (13)$$

reducing to the exact answer $a_G^{\text{exact}} = 1 - \frac{n}{2}$ as $\lambda \rightarrow 1$.

Alternately, we could expand the \mathcal{G} in powers of λ , a procedure we followed in [6,49]. We expanded \mathcal{G} out to first order in λ from Eq. (7) since that already gives the required $O(\lambda^2)$ correction. Thus, we set $\mathcal{G} = \mathbf{g}(1 - \lambda n/2) + O(\lambda^2)$, where the sum rule Eq. (12) was used for evaluating $\sum_{k, \omega_n} \mathbf{g}(k)$. As a result, we obtain the approximate result

$$a_G^{(II)} = 1 - \lambda \frac{n}{2} + \lambda^2 \frac{n^2}{4} + O(\lambda^3). \quad (14)$$

Setting $\lambda \rightarrow 1$, we thus get two alternate approximate skeleton versions of Eq. (7):

$$\mathcal{G}^{(I)}(k, i\omega_n) = \mathbf{g}^{(I)}(k, i\omega_n) \{1 - n/2 + \Psi(k, i\omega_n)\}, \quad (15)$$

$$\begin{aligned} \mathcal{G}^{(II)}(k, i\omega_n) &= \mathbf{g}^{(II)}(k, i\omega_n) \\ &\quad \times \{1 - n/2 + n^2/4 + \Psi(k, i\omega_n)\}, \end{aligned} \quad (16)$$

where both expressions involve *the same* approximate Ψ given in Eq. (10), and the auxiliary $\mathbf{g}^{(\dots)}$ is also adjusted to have the appropriate expression for a_G in Eq. (8). This dichotomous situation arises due to the composite nature of the physical \mathcal{G} , whereas in standard many-body problems the skeleton expansion is unique.

In [6] as well as [49] we employed Eq. (16) to compute the electron self-energy and spectral functions. It was argued that this expression should be valid for low-particle density $n \lesssim 0.7$. In [6], the results were compared with the numerically exact DMFT results for the same model. It was found that the self-energy is indeed close to the exact answer in the low-density limit. At the other end of *high densities* $n \lesssim 1$, it was found that the self-energy is also very close to the exact result, provided we scale the frequencies by the quasiparticle weight Z of that theory. This remarkable observation shows that in ECFL theory, the Dyson self-energy (6) found by compounding two simpler expressions χ and ψ , has the correct functional form. Moreover, the unusual and important feature of particle-hole asymmetry, i.e., the presence of a strong ω^3 term in the $\text{Im} \Sigma$, comes about “naturally” within the scheme. This feature has been argued to be generic for strongly correlated systems, as argued in [8] and in the closely related [5] for the Anderson impurity model. The need for rescaling the frequency arises because the computed $Z^{(II)}$ using the approximate version (16) overestimates this variable as n increases beyond the estimated limit of $n \sim 0.7$. We see in [6] (Fig. 16) that $Z^{(II)}$ does not even vanish as $n \rightarrow 1$, as one expects in a Mott insulator.

Within the spirit of Eq. (16) one might expect that further approximations involving higher-order terms in λ will enhance the range of validity in density. Such a program is essentially numerically intensive since beyond second order, one needs to use other techniques, such as Monte Carlo generation and evaluation of diagrams [50–52]. We are currently performing these calculations, and have made formal progress towards this goal in [46], by enumerating the nontrivial diagrammatic rules in this model. The diagrams that we encounter include and go beyond Feynman diagrams, as necessitated by the lack of Wick's theorem in the noncanonical theory.

On the other hand, the analytical ease of the second-order theory offers considerable advantage relative to other contemporary methods. For low orders in λ most calculations can be done by hand, and the remaining computations are modest in scope. Analytical methods also have a much greater flexibility: they can be applied in lower dimensions as well. Further, the agreement with the other methods (DMFT [13–39], numerical renormalization group [5]) and also experiments on ARPES for the electron line shapes [7] is very good. In view of these positive factors, it appears to be useful to examine if the problem with the quasiparticle weight $Z^{(II)}$ at $n \lesssim 1$ can be understood and corrected, making other necessary approximations along the way. This is indeed the purpose of this paper; we will see below that the approximation (15) provides us with the correct direction for such an approach.

III. SUM RULES NECESSARY FOR THE VANISHING OF Z NEAR THE MOTT INSULATING STATE

Let us first understand the factors that make Z vanish as we approach the Mott insulating limit. For this purpose, it is useful to recall the local density of states of the Hubbard model for the case of a sufficiently large U (see [53] for a useful discussion). Here, we expect the formation and clear separation of characteristic lower and upper Hubbard bands, as indicated in the schematic Fig. 2. Specializing to $T = 0$ for simplicity,

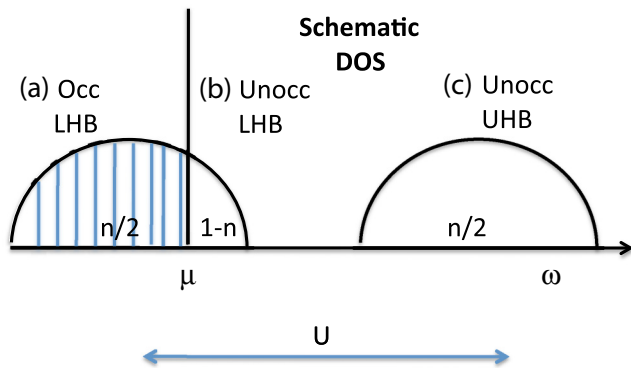


FIG. 2. A schematic depiction of the local spectral density of states $\rho_{G,Local}(\omega)$ [popularly called $A_{Local}(\omega)$] for the large- U Hubbard model, where the correlation split Hubbard bands are clearly separated. It shows three regions: (a) occupied electronic states, (b) unoccupied lower Hubbard band states, and (c) unoccupied upper Hubbard band states, with their respective weights as in Eq. (18). The t - J model sends the region (c) off to infinity with weights given in Eq. (19). The area in region (b) is exactly $(1 - n)$, and preserving this in an approximation is key to obtaining the correct low-energy scale.

we note that for the Hubbard model with $n < 1$, the spectral weight for the local $\rho_G(\omega)$ of the physical electron satisfies the unitary sum rule $\int d\omega \rho_G(\omega) = 1$. We use a notation where a sum over \vec{k} is implied for unlabeled functions (without the \vec{k} argument), e.g., $\rho_G(\omega) \equiv \sum_{\vec{k}} \rho_G(\vec{k}, \omega)$. The local Green's function itself is given by

$$G(\omega + i0^+) = \int dv \frac{\rho_G(v)}{\omega - v + i0^+}, \quad (17)$$

and so the $\omega \rightarrow \infty$ asymptotic behavior is determined by this sum rule as $G(\omega) \rightarrow \frac{\int dv \rho_G(v)}{\omega} = \frac{1}{\omega}$. This can be partitioned into three sum rules as depicted in Fig. 2:

$$\begin{aligned} \int_{-\infty}^0 d\omega \rho_G(\omega) &= n/2, & \int_0^{\Omega_*} d\omega \rho_G(\omega) &= 1 - n, \\ \int_{\Omega_*}^{\infty} d\omega \rho_G(\omega) &= n/2, \end{aligned} \quad (18)$$

where Ω_* is an energy scale denoting the upper end of the lower Hubbard band and hence is $\sim O(W)$; it is well defined provided $U \gg W$. As stated, these three integrals add up to 1, ensuring that a full electron is captured. On the other hand, the t - J model spectral function $\rho_G(\omega)$ satisfies

$$\int_{-\infty}^0 d\omega \rho_G(\omega) = n/2, \quad \int_0^{\infty} d\omega \rho_G(\omega) = 1 - n, \quad (19)$$

where the upper Hubbard band (and Ω_*) is pushed off to $+\infty$, and thus the occupied and unoccupied portions add up to $1 - n/2$. This can be visualized clearly with the help of Fig. 2. This argument also determines the $\omega \rightarrow \infty$ asymptotic form $\lim_{\omega \rightarrow \infty} \mathcal{G}(\omega) \rightarrow \frac{1-n/2}{\omega}$, and gives us a relation of importance to this study:

$$\left(\lim_{\omega \rightarrow \infty} \mathcal{G}(\omega) \rightarrow \frac{1-n/2}{\omega} \right) \leftrightarrow \left(\int_0^{\infty} d\omega \rho_G(\omega) = 1 - n \right). \quad (20)$$

To see its relevance, we note that as $n \rightarrow 1$, the chemical potential increases towards the top of the lower Hubbard band. This implies that the unoccupied portion of the lower Hubbard band shrinks to zero. Since roughly half of the quasiparticle's weight [54] resides in this shrinking energy domain of $O(1 - n)$ times the bandwidth, the quasiparticle residue Z must vanish at least as fast as $O(1 - n)$.

We may now refer back to Eq. (16); since from the definitions (10) and (11) we can see that $\lim_{\omega \rightarrow \infty} (\Psi(\omega), \chi(\omega)) \rightarrow 0$ and also $\lim_{\omega \rightarrow \infty} \mathbf{g}(\omega) \rightarrow \frac{1}{\omega}$, we combine these to obtain

$$\lim_{\omega \rightarrow \infty} \mathcal{G}^{(II)}(\omega) \rightarrow \frac{1 - n/2 + n^2/4}{\omega},$$

whereby the unoccupied region $\int_0^{\infty} d\omega \rho_{G^{(II)}}(\omega) = 1 - n + n^2/4$, in conflict with the condition (20) for a vanishing Z , as $n \rightarrow 1$.

Having thus identified this weakness of the approximation, we also see by the same argument that Eq. (15) would automatically give us a vanishing Z , as $n \rightarrow 1$; the factors are now appropriate for the condition (20) to hold.

IV. CUTOFF SECOND-ORDER ECFL THEORY

Motivated by the above discussion, we now implement a skeleton graph expansion, where the basic atoms, or units, are still \mathbf{g} , but in static terms involving \mathcal{G} , such as in Eq. (9), we use the exact particle-number sum rule (12). This leads us to study the equations in Eq. (15).

A. Full set of self-consistent equations

For convenience and future reference, we summarize the full set of equations to be solved self-consistently. These are similar to the ones used in [6,49] with all the necessary changes for the present case made. The band density of states is taken as the semicircular expression $D(\epsilon) = 2/(\pi D)\sqrt{1 - (\epsilon/D)^2}$, and thus $2D$ is the bare bandwidth. The complex frequency is denoted as $z = \omega + i0^+$, the local Green's function and its energy moments are defined by

$$\mathbf{g}^{-1}(\epsilon, z) = z + \mu' - (\epsilon - u_0/2) \left(1 - \frac{n}{2} + \Psi_{[1]}(z) \right) - \chi_{[1]}(z), \quad (21)$$

$$\mathbf{g}_{Loc,m}(z) = \int d\epsilon D(\epsilon) \mathbf{g}(\epsilon, z) \epsilon^m = \int dv \frac{\rho_{gL,m}(v)}{z - v}. \quad (22)$$

The chemical potential μ' absorbs all constants such as $\chi_{[0]}$, leading to

$$\mu = \mu' + \frac{u_0}{2} \left(1 + \frac{n}{2} \right) - \int d\omega f(\omega) \rho_{gL,1}(\omega), \quad (23)$$

where $f(\omega) = 1/(1 + \exp \beta\omega)$ is the Fermi function and we will need below $\bar{f} = 1 - f$. Equation (22) serves to introduce the spectral functions $\rho_{gL,m}(v)$; these are most often computed from the reversed relation

$$\rho_{gL,m}(\omega) = -\frac{1}{\pi} \text{Im} \mathbf{g}_{Loc,m}(\omega + i0^+). \quad (24)$$

The physical Green's function is found from $\mathcal{G}(\epsilon, z) = [1 - n/2 + \Psi(z)] \times \mathbf{g}(\epsilon, z)$, and the Dyson self-energy from $\Sigma(z) = z + \mu - \epsilon - \mathcal{G}^{-1}(\epsilon, z)$. We define its local version $\mathcal{G}_{Loc}(\omega)$ and its density through a band integration

$$\mathcal{G}_{Loc,m}(z) = \int d\epsilon D(\epsilon) \epsilon^m \mathcal{G}(\epsilon, z),$$

$$\rho_{gL,m}(\omega) = -\frac{1}{\pi} \text{Im} \mathcal{G}_{Loc,m}(\omega + i0^+). \quad (25)$$

The physical momentum-integrated spectral function $\rho_{gL,0}$ is an object of central interest. It is also needed for the number sum rule below Eq. (30). The computation of \mathbf{g} requires the two complex self-energies Ψ, χ . These can in turn be found from expressions involving the fundamental convolution:

$$\rho_{abc}^{(I)}(u) = \int_{u_1, u_2, u_3} \delta(u + u_3 - u_1 - u_2) \{ f(u_1) f(u_2) \bar{f}(u_3) + \bar{f}(u_1) \bar{f}(u_2) f(u_3) \} \rho_{gL,a}(u_1) \rho_{gL,b}(u_2) \rho_{gL,c}(u_3), \quad (26)$$

where the right-hand side is conveniently computed from the local densities $\rho_{gL,a}$, by using fast Fourier transforms.

This density is required for $(a,b,c) = 0,1$, and determines the complex function

$$\mathcal{I}_{abc}(z) = \mathcal{P} \int dv \frac{\rho_{abc}^{(I)}(v)}{z - v}. \quad (27)$$

From this object, the two self-energies can be found as the combinations

$$\Psi_{[1]}(z) = 2\mathcal{I}_{010}(z) - u_0 \mathcal{I}_{000}(z),$$

$$\chi_{[1]}(z) = 2\mathcal{I}_{011}(z) - u_0 [\mathcal{I}_{010}(z) + \mathcal{I}_{001}(z)] + \frac{u_0^2}{2} \mathcal{I}_{000}(z). \quad (28)$$

In summary, we can compute \mathbf{g} in terms of χ, Ψ from Eq. (21). Having done so, we compute χ, Ψ in terms of the \mathbf{g} from Eq. (28), thus defining the second part of the loop. The two chemical potentials μ and u_0 are found from Eq. (23) and the two particle-number sum rules:

$$\int d\omega f(\omega) \rho_{gL,0}(\omega) = \frac{n}{2}, \quad (29)$$

$$\int d\omega f(\omega) \rho_{gL,0}(\omega) = \frac{n}{2}, \quad (30)$$

thereby all variables can be self-consistently calculated through a simple iterative scheme. The only inputs are the density of particles n and the temperature T .

B. Considerations of high density $n \rightarrow 1$ at low T , and the entropy at high T

Before discussing the results, we note an important constraint that arises when we study the theory at high temperatures. We need to make sure that the number of states after the Gutzwiller projection has the correct value; this requires that the chemical potential has the correct asymptotic value at high T . When $T \gg t, J$ the chemical potential grows linearly with T . From simple considerations of the atomic limit $t = 0 = J$, one can calculate the partition function exactly, from this one finds

$$\mu \sim k_B T \ln \{ n / [2(1 - n)] \}, \quad (31)$$

where N_s and $n = N/N_s$ are the number of sites and the density, respectively. This linear growth with T with the correct coefficient also ensures that the entropy near the Mott limit is correctly reproduced at high T . Upon using the Maxwell relation $(\partial S / \partial N) / T = -(\partial \mu / \partial T)_N$, and the initial condition $S(n \rightarrow 0) = 0$, we find

$$S \sim -k_B N_s \{ n \ln n / 2 + (1 - n) \ln(1 - n) \}, \quad (32)$$

a well-known result. We must therefore also ensure that the approximation satisfies this condition (31), in order to obtain the correct entropy at high T .

Upon solving Eqs. (21)–(30) at high densities $n \gtrsim 0.8$ as $T \rightarrow 0$, or high $T \gg D$ with moderated densities $n \gtrsim 0.7$, we find that in each case the spectral function tends to flatten out on the occupied side, extending in range to $\omega \ll -D$ with little weight in the tails. For the high- T case, a second consequence is that the computed slope $d\mu/dT$ begins to depart from Eq. (31). The flattening is consequence of the

growth of u_0 which also increases linearly with T , becoming larger than the bandwidth $2D$, as seen in Fig. 5. This growth enhances the coefficients in the self-energies Eq. (28) and pushes one into a strong u_0 regime, unless we impose some cutoff. In the $T \rightarrow 0$ limit, the exact numerical results for spectral functions from DMFT [6] do confirm the expectation of a compact support for the spectral function, and hence the observed growth is artificial.

C. Cutoff scheme with a Tukey window

We saw above that two physically distinct regimes involving different types of physics, namely, the high- T regime at any density and the high-density regime at low T , share the common problem of growing tails of the spectral function.

In order to control this unphysical growth in both cases, we need to impose an appropriate high-energy cutoff. Higher-order terms in the λ expansion are expected to eliminate this growth in a systematic way, without needing an extra prescription. A detailed analysis of the cutoff issue within the λ expansion is underway currently, and we expect to present the details in a forthcoming paper. However, at the level of the lowest-order approximations, it seems that we do need to impose an extra cutoff, thereby introducing one more approximation. A rough estimate of the cutoff can be made by observing that the self-energy calculated by using the bare \mathbf{g}_0 (setting $\chi \rightarrow 0$ and $\Psi \rightarrow 0$) in Eq. (26) would give the spectral weights a width of maximum range $\pm 3D$; by setting $u_1 = D$, $u_2 = D$, $u_3 = -D$, we satisfy one of the Fermi combinations with $u \sim 3D$. By flipping signs we can reach $u = -3D$, thus, a range of frequencies $-3D \leq \omega \leq 3D$ is feasible. The region near $|\omega| \sim 3D$ would then be in the tails of the function. In a skeleton expansion, on the other hand, with increasing interaction strength u_0 , we have the possibility of a runaway growth since under first iteration, the computed $\rho_{\mathbf{g}L}$ can now extend to $\pm 3D$ as compared to the range $\pm D$ of the bare density, and so forth. Hence, one plausible strategy would be to limit the growth of the auxiliary spectral functions to a range $\pm c_0$, with $c_0 \sim 2D$, with the physical spectral functions possibly extending somewhat beyond this. Since two very different regimes, that of high T and high density are involved, we can test the additional approximations self-consistently, and thereby avoid unduly biasing the results.

It appears reasonable to choose the high-energy cutoff by requiring that we obtain the known high- T slope and therefore the high- T entropy (32) at all densities. While it might be possible to obtain the exact entropy by adjusting the cutoffs at each density separately, we content ourselves by finding a reasonable global fit instead, i.e., one set of *density-independent cutoffs* yielding the roughly correct entropy at relevant densities. The high- T entropy is estimated at $T \lesssim 1$. It should be noted that $T \sim 1$ is not always in the high- T limit, especially for the tricky region close to $n \sim 2/3$ where we know that $d\mu/dT$ vanishes at high T from Eq. (31), hence, it is expedient to limit the high- T region to $T \lesssim 1$. Having chosen such a cutoff, one can then explore the other physically interesting domain, and study the spectral functions at low T in the energy range $|\omega| \lesssim D$. This is a low-energy scale compared to the cutoffs, but already a very high-energy scale, in comparison to the physically interesting regimes $|\omega| \lesssim \frac{D}{3}$

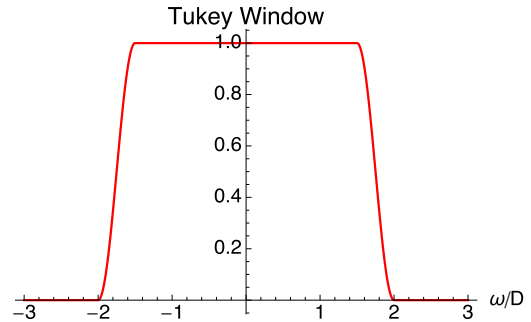


FIG. 3. Multiplication through the Tukey window $\mathbf{W}_T(\omega)$ [Eq. (34)] is used for providing a cutoff in our scheme (33). It is applied only to the auxiliary local Green's function $\rho_{\mathbf{g}L,m}(\omega)$, while the physical spectral functions $\rho_{\mathbf{g}L}(\omega)$ are unconstrained, apart from an overall window $|\omega| \leq 5D$ used for numerical purposes. In this work, the upper cutoff used is $\Omega_c^{(+)} = 2D$, and the lower cutoff $\Omega_c^{(-)} = 1.5D$.

or even lower. We find below that the low- T spectra indeed are better behaved with the cutoff. The low-energy results presented here are quite insensitive to the details of the choice for the cutoff, and hence one might be reasonably confident that the answers are not unduly biased by the choice made.

The method employed for imposing the high-energy cutoff was arrived at after some experimentation. We multiply the local spectral function (24) by a Tukey window function used in data filtering:

$$\hat{\rho}_{\mathbf{g}L,m}(\omega) = \frac{1}{\mathcal{V}} \rho_{\mathbf{g}L,m}(\omega) \mathbf{W}_T(\omega), \quad (33)$$

where the constant \mathcal{V} is found from the normalization condition $\int \hat{\rho}_{\mathbf{g}L,0}(\omega) d\omega = 1$. Here, the smooth Tukey window $\mathbf{W}_T(\omega)$ is unity over the physically interesting, i.e., feature-rich frequency domain $|\omega| \leq \Omega_c^{(-)}$, where it starts falling off smoothly, and vanishing beyond the high-frequency cutoff $|\omega| = \Omega_c^{(+)}$. It is defined as a piecewise function (see Fig. 3)

$$\begin{aligned} \mathbf{W}_T(\omega) &= 1 \quad \text{for } \Omega_c^{(-)} \geq |\omega| \\ &= \frac{1}{2} \left(1 + \sin \left\{ \pi/2 \frac{\Omega_c^{(+)} + \Omega_c^{(-)} - 2|\omega|}{\Omega_c^{(+)} - \Omega_c^{(-)}} \right\} \right) \\ &\quad \text{for } \Omega_c^{(+)} \geq |\omega| \geq \Omega_c^{(-)} \\ &= 0 \quad \text{for } |\omega| > \Omega_c^{(+)}. \end{aligned} \quad (34)$$

This procedure involves a *single rescaling*: after computing the local spectral functions $\rho_{\mathbf{g}L,m}$ (with $m = 0, 1$) from the self-energies as in Eq. (24), we multiply with \mathbf{W}_T and rescale as in Eq. (33) before sending the result back into the self-energy calculation in Eq. (28). Note that the prescription (33) involves the auxiliary local Green's function $\mathbf{g}_{L,m}$ which is the basic building block in the theory. The cutoff is imposed *only* on $\rho_{\mathbf{g}}$ in Eq. (24), and the other spectral functions are then computed by the unchanged equations (21)–(30).

We chose the parameters $\Omega_c^{(+)} = 2D$, and the lower cutoff $\Omega_c^{(-)} = 1.5D$ after some experimentation. This choice of the cutoffs is in accord with the discussion above where we concluded $c_0 \sim 2D$. With this cutoff and rescaled auxiliary Green's function, the physical spectral function $\rho_{\mathbf{g}}$ is computed as per the rules without any further assumptions. It typically

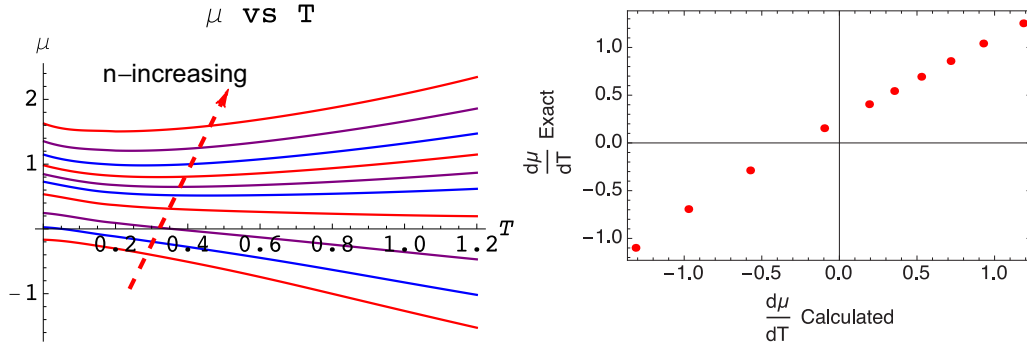


FIG. 4. Left: The chemical potential at particle densities $n = 0.4, 0.5, 0.6, 0.7, 0.75, 0.775, 0.8, 0.825, 0.85, 0.875$ increasing from bottom to top. We confine ourselves to the limited regime $T \leq 1.2$ since higher T requires further adjustment of the cutoffs. Note that within this regime, the $\mu(T)$ curve turns around at a density around $n \sim 0.7$. For lower densities, μ decreases monotonically with increasing T , whereas at higher densities we have a shallow minimum followed by a regime of rising μ . This change of behavior is expected from Eq. (31), and has important physical consequence of changing the sign of the Kelvin thermopower for correlated matter [55]. Right: The slope $d\mu/dT$ is calculated from the $\mu(T)$ curves at $T = 1$, and contrasted with the exact values from Eq. (31). The points are taken from the same set of particle densities n as the figure on left, increasing from left to right. Since there is yet some curvature in the figures at left when $T = 1$, our procedure provides only a rough estimate. We note that these are in fair correspondence, especially at low hole density (see top right quadrant).

does extend to about $4.5D$ or $5D$ on the occupied side, but not beyond this scale. For numerical purposes, we also use an upper cutoff for the physical spectral function range as $\sim 5D$, this energy corresponds to Ω_* in Fig. 2.

V. RESULTS FOR CHEMICAL POTENTIAL, QUASIPARTICLE WEIGHT, SELF-ENERGY, AND SPECTRAL FUNCTIONS

A. Chemical potential and quasiparticle weight Z

With the chosen cutoff, we examine the chemical potential as a function of density and T in Fig. 4. We observe in the left panel of Fig. 4 that the chosen cutoff provides a reasonable description of the μ versus T curves at different densities. These exhibit an upturn between $n = 0.6$ and 0.7 in the T domain that is computationally reliable within this scheme. The right panel of Fig. 4 shows that the slope $d\mu/dT$ is also in reasonable agreement with the exact answer for this slope, apart from some error near the difficult regime of $n \sim \frac{2}{3}$. Here, we know from Eq. (31) that the slope is zero at high enough T and this causes problems of convergence.

We examine the various pieces adding up to the chemical potential in the right panel of Fig. 5. These curves also show that the Mott-Hubbard physics of the upturn of $\mu(T)$ is enforced by the u_0 term, it is thus quite crucial within this formalism. We also note that calculations without the cutoff lead to much larger values of u_0 .

Overall, it seems that the results for μ are quite reasonable in the hole-rich region $n \geq 0.75$ (i.e., $\delta \leq 0.25$) with the global choice made, i.e., without requiring a fine tuning of the cutoffs with the density. We therefore proceed to use this for computing the spectral functions, and other physically interesting variables, also evaluated in the complementary low- T region.

Turning to the main objective of this work of calculating the correct energy scale near the Mott limit, we display the computed Z versus the hole density $\delta = 1 - n$ in the left panel of Fig. 6. It is interesting that the values obtained are significantly better than those reported in [6], we now find

Z vanishes as $\delta \rightarrow 0$. The solid line gives the numerically exactly determined Z from DMFT, which is extremely well fit by $Z \sim \delta^{1.39}$. This latter behavior is noteworthy in that it vanishes faster than linear in δ . The ‘‘mean field descriptions’’ involving slave auxiliary particles as well as the Brinkman-Rice theory [56] of the correlated metallic state give a linear $Z \propto \delta$. Therefore, this result indicates the need to account for fluctuations beyond the mean field description. It is interesting that the present calculation also gives a nonlinear behavior, with a slightly larger exponent than 1.39. We plan to return to a closer analytical study of this interesting result, obtained from the numerics of our solution.

B. Self-energy and spectral functions at low T

We have also studied the quasiparticle decay rate at $T \sim 0$, defined for $|\omega| \leq ZD$ through a Fermi liquid form with the expected particle-hole asymmetric correction [8]

$$-\text{Im}\Sigma(\omega) = \frac{\omega^2}{\Omega_0} \left(1 - \frac{\omega}{\Delta} \right), \quad (35)$$

whereby introducing two energies: Ω_0 , which determines the magnitude of $\text{Im}\Sigma$ and Δ the asymmetry scale. In [6] and also in [5], it was pointed out that Ω_0 varies like Z^2 near the Mott insulating limit, leading to a scaling of the Green’s function frequency with Z at low energies. In this work, the Ω_0 is computed by averaging $\text{Im}\Sigma(\omega)$ in the domain $|\omega| \leq ZD$. In the bottom right panel of Fig. 7, we show the variation of Ω_0 versus Z^2 and in the inset with δ^2 . Since we have seen nonlinear corrections in Z as seen in Fig. 6, these two plots seem to support more closely the scaling of Ω_0 with Z^2 , rather than δ^2 at the lowest δ . It seems possible to improve the agreement by choosing a density-dependent cutoff, however, the global cutoff already achieves fair agreement.

In the top left panel of Fig. 7, we plot $-\text{Im}\Sigma$ versus ω/Z at different densities. As already noted in [6], these curves fall on top of each other quite well. The curves also exhibit particle-hole asymmetry as noted before [2,8]. This is exhibited by decomposing the $\text{Im}\Sigma$ into symmetric and

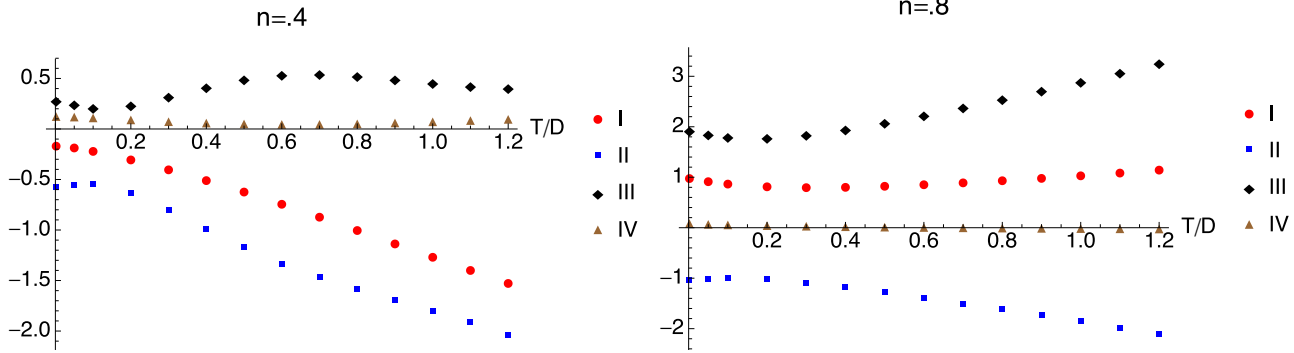


FIG. 5. The T dependence of the chemical potential μ and its three additive contributions from Eq. (23) at two densities. The physical chemical potential μ (I, red), the auxiliary part: μ' (II, blue), the u_0 contribution: $(1/2 + n/4)u_0$ (III, purple), and the small part from the integral $-\int f\rho_{gL,1}$ (IV, magenta). The observed upturn in μ at high T for $n = 0.8$, reflecting the physics of Mott holes near half-filling, is predominantly due to the upturn of the second chemical potential u_0 . Its growth, in turn, causes the numerical issues requiring the implementation of a cutoff in this work.

antisymmetric components in the top right and bottom left panels. The antisymmetric part can be analyzed to read off the energy scale Δ in Eq. (35). We find that Δ is proportional to Z again, but with a weak density-dependent correction:

$$\Delta(\delta) = Z(\delta)\{3.38 - 15.6\delta + 27.1\delta^2\}. \quad (36)$$

The region beyond the straight line is captured on average, by extending Eq. (35) to

$$-\text{Im}\Sigma(\omega) = \frac{\omega^2}{\Omega_0} \left(1 - \frac{\omega}{\Delta\sqrt{1 + 2\omega^2/Z^2}} \right). \quad (37)$$

This expression is potentially useful for phenomenological extensions of the theory.

In Figs. 8 and 9, we display the raw unscaled spectral functions and the imaginary part of the self-energy for various physical parameters. In Fig. 8, the low- T spectra are shown at different densities. Note that the significant range of ω where the spectral functions and self-energy vary, shrinks rapidly

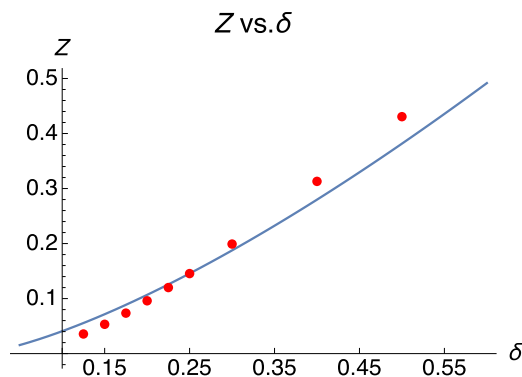


FIG. 6. The computed quasiparticle weight Z (dots) versus the hole density $\delta = 1 - n$, compared with the exact numerical results from DMFT ([6] solid curve), which fits very well to the formula $Z \sim \delta^{1.39}$. We see that the present scheme accounts well the suppression of Z near $\delta \sim 0$, even reproducing nonlinear vanishing near the Mott limit seen in [6]. This nonlinear feature goes beyond the predictions of both slave-boson mean field and Brinkman-Rice theory [56], and signifies an important correction to the mean field behavior.

with increasing n ; this is indirectly a reflection of variation of the Z with density in Fig. 6 since the scale of variation of Σ is set by Z . We also note that the spectral asymmetry in $\text{Im}\Sigma$ is very clearly visible here.

C. Temperature variation of the self-energy and spectral functions

In Fig. 9, we display the T dependence of the spectral function and the self-energy. One of the advantages of our computational scheme is the ease with which T variation can be computed. We are thus able to obtain easily the crossover from a coherent (extremely correlated) Fermi liquid regime at low T to an incoherent nondegenerate correlated state. The spectral function peaks rapidly broaden and shift as the temperature is increased. We also note that the Fermi coherence, signaled by a small magnitude of $\text{Im}\Sigma$ at small ω , is rapidly lost on heating, leading to a flat and structureless function. A comparison of the curves at $n = 0.85$ and 0.875 shows that in this range of densities, where the Z is already very small, the effective Fermi temperature is also diminished since the same (small) variation of T produces a relatively large change in the damping.

VI. TEMPERATURE DEPENDENCE OF RESISTIVITY AND RELATED QUANTITIES

Perhaps the single most important characterization of a theory is via the resistivity. It is a notoriously hard object to calculate reliably, and yet one that is most sensitive to the lowest-energy excitations of the system. Since we have argued that the present version of ECFL captures the low-energy excitations of the electron, it is useful to examine its results for resistivity for the t - J model in infinite dimensions, or equivalently the $U = \infty$ Hubbard model. The resistivity has been calculated numerically from DMFT quite recently in two papers [42,43], and hence it is of interest to see how our analytical calculation compares with these exact results.

We start with the Kubo expression for resistivity, with the vertex correction thrown out, thanks to the simplification

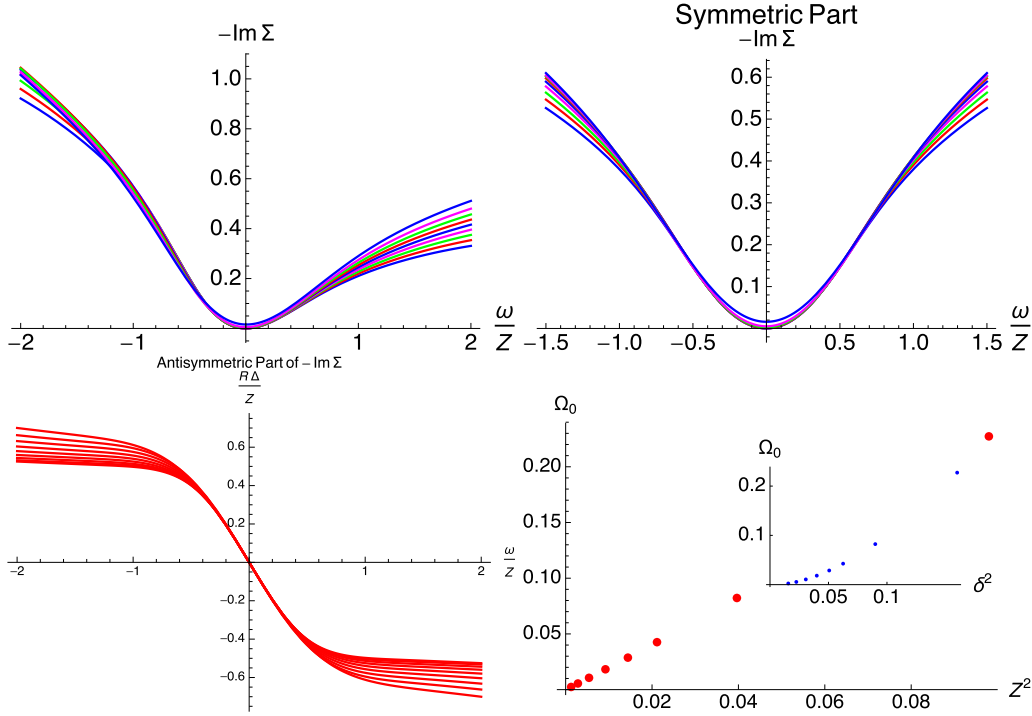


FIG. 7. Top left: $-\text{Im}\Sigma(\omega)$ versus ω/Z at several densities $n = 0.7, 0.725, 0.75, 0.775, 0.8, 0.825, 0.85, 0.875, 0.9$ from bottom to top. We see that the frequency dependence scales well with Z , with better behavior on the occupied side $\omega \leq 0$. Top right: The symmetrized function $[-\Sigma''(\omega) - \Sigma''(-\omega)]/2$ exhibits the quadratic behavior at $\omega \sim 0$ expected from a Fermi liquid. Bottom left: The antisymmetric part is defined as $R = [\Sigma''(\omega) - \Sigma''(-\omega)]/[\Sigma''(\omega) + \Sigma''(-\omega)]$, so that if we assume Eq. (35) then $R = -\omega/\Delta$. We show the computed R multiplied by Δ/Z at the above densities versus ω/Z , with $n = 0.9$ at the top and $n = 0.7$ at the bottom for $\omega \leq 0$. These collapse to a straight line with slope -1 in the range $|\omega| \leq Z$, provided we allow for an additional mild density dependence of the ratio Δ/Z , as in Eq. (36). Bottom right: The energy scale Ω_0 [Eq. (35)] determining the magnitude of the $\text{Im}\Sigma$ at $T = 0$ is shown versus Z^2 , and in the inset versus the hole density δ^2 . Here, Ω_0 is seen to scale better with Z^2 rather than with δ^2 .

arising from $d \rightarrow \infty$:

$$\sigma_{DC} = \frac{2\pi\hbar e^2}{V} \sum_k (v_k^x)^2 \int d\omega (-\partial f/\partial\omega) \rho_G^2(\epsilon_k, \omega), \quad (38)$$

where the band velocity is given as $\hbar v_k^x = \partial\epsilon_k/\partial k_x$. We wrap the velocity into a useful function

$$\begin{aligned} \Phi(\epsilon) &= \frac{1}{a_0} \frac{1}{N_s} \sum_k \delta(\epsilon - \epsilon_k) (v_k^x)^2 / a_0^2 \\ &= \frac{1}{a_0} D(\epsilon) \left\langle \frac{(v_k^x)^2}{a_0^2} \right\rangle_{\epsilon_k = \epsilon}, \end{aligned} \quad (39)$$

where a_0 is the lattice constant in the hypercubic lattice, and N_s the number of sites and we use the Bethe lattice semicircular density of states $D(\epsilon) = \frac{2}{\pi D} \sqrt{1 - \epsilon^2/D^2}$. Deng *et al.* [42,57] calculate that

$$\frac{\Phi(\epsilon)}{\Phi(0)} = \Theta(1 - \epsilon^2/D^2)^{3/2} \sqrt{1 - \epsilon^2/D^2}, \quad (40)$$

where $\Phi(0)$ is absorbed into a constant $\sigma_0 = e^2 \hbar \Phi(0)/D$, which is identified with the Ioffe-Regel-Mott conductivity. With this choice of the vertex we obtain

$$\sigma_{DC} = \sigma_0 2\pi D \iint d\epsilon d\omega (-\partial f/\partial\omega) \left(\frac{\Phi(\epsilon)}{\Phi(0)} \right) \rho_G^2(\epsilon, \omega). \quad (41)$$

We write the (inverse) Green's function at real ω as

$$\mathcal{G}_{\pm}^{-1}(\epsilon, \omega) = A(\omega) - \epsilon \pm iB(\omega), \quad (42)$$

where the retarded case corresponds to \mathcal{G}_+ , and

$$\begin{aligned} A(\omega, T) &= \omega + \mu - \text{Re} \Sigma(\omega, T), \\ B(\omega, T) &= \pi \rho_{\Sigma}(\omega, T) = -\text{Im} \Sigma(\omega, T), \end{aligned} \quad (43)$$

and Σ is the Dyson self-energy. Setting $D = 1$ and using the identities $\rho_G = i/(2\pi)(\mathcal{G}_- - \mathcal{G}_+)$ and $\mathcal{G}_{\pm}^2 = \partial_{\epsilon} \mathcal{G}_{\pm}$, and further integrating by parts over ϵ we obtain

$$\begin{aligned} \sigma &= \sigma_0 \int d\omega (-\partial f/\partial\omega) \xi(\omega), \\ \xi(\omega) &= \frac{1}{2\pi} \int d\epsilon \left\{ \frac{i}{B} (\mathcal{G}_+ - \mathcal{G}_-) \frac{\Phi(\epsilon)}{\Phi(0)} + (\mathcal{G}_+ + \mathcal{G}_-) \frac{\Phi'(\epsilon)}{\Phi(0)} \right\}. \end{aligned} \quad (44)$$

Using the explicit form of Φ and \mathcal{G}_{\pm} , we reexpress ξ exactly as

$$\xi(\omega) = \frac{1}{\pi} \int_{-1}^1 d\epsilon \sqrt{1 - \epsilon^2} \frac{1 - 3\epsilon A + 2\epsilon^2}{B^2 + (A - \epsilon)^2}. \quad (45)$$

The evaluation of this integral is straightforward, and leads to a cumbersome result. A simple answer for the leading behavior when $B \ll 1$ can be found, provided $(A - \epsilon)$ goes through zero in the interval of integration. Since we will see that $|A| \ll 1$ for

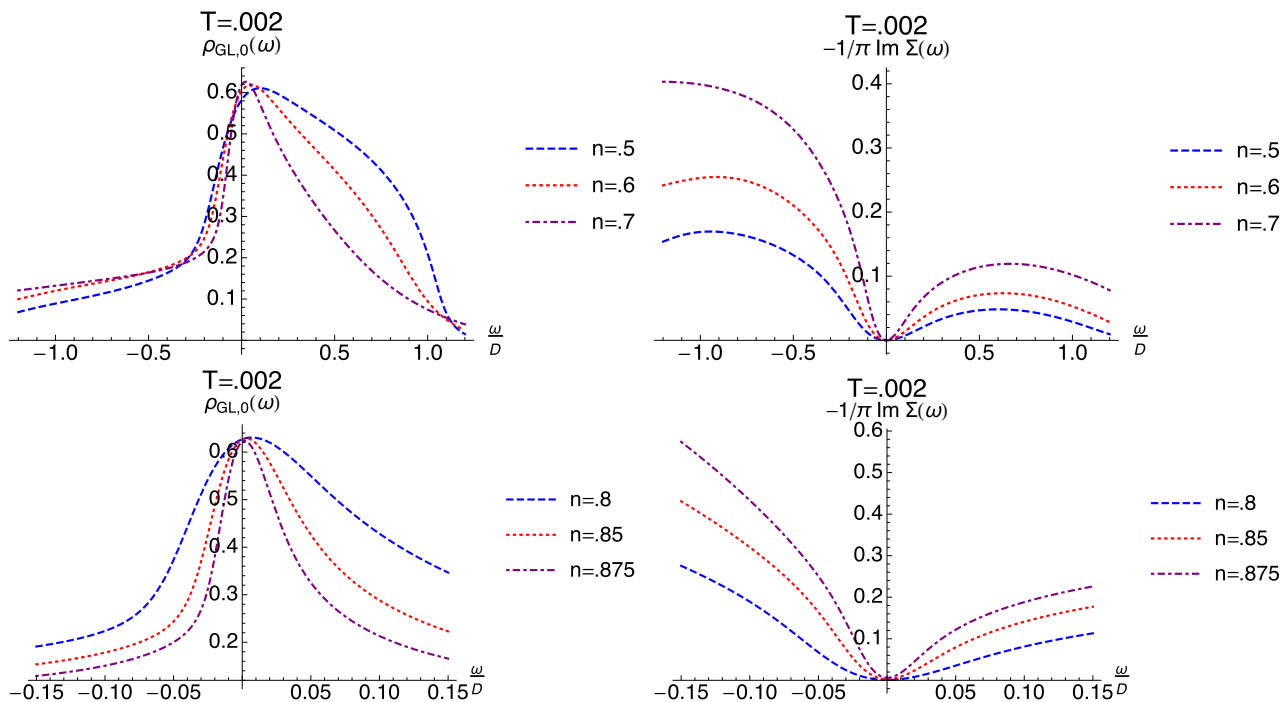


FIG. 8. The two figures on the left display the physical local spectral function $\rho_{GL,0} = -\frac{1}{\pi} \text{Im} \mathcal{G}_{Loc,0}(\omega + i0^+)$ from Eq. (25), and the two figures on the right show the Dyson self-energy $-\frac{1}{\pi} \text{Im} \Sigma(\omega)$, plotted against the frequency ω/D . The figures are at low T for the six indicated values of the density, and display a region that is somewhat greater than the one, where it is expected to be reliable $|\omega| \lesssim ZD$. One sees a correlation between the quasiparticle weight Z (Fig. 6) and the scale of variation of the decay rate. Densities $n > 0.875$ have larger errors in Z compared to the exact DMFT results (see Fig. 6), and therefore not shown. However, it is easy to picture them at low ω , using the observation that scaling ω with Z collapses Σ' .

all temperatures and frequencies of interest ($\omega \sim 0, \frac{T}{D} \lesssim 0.3$), this will always be the case. We may write $\epsilon = A + B \tan(\theta)$, retain the leading terms for small B , and set $B \rightarrow 0$ in the remainder. With this, we obtain the asymptotic approximation

$$\lim_{B \ll 1} \xi(\omega) \sim \frac{[1 - A^2(\omega)]^{3/2}}{B(\omega)} \Theta[1 - A^2(\omega)]. \quad (46)$$

In Fig. 10, we use Eq. (46) to plot $\frac{\rho_{dc}}{\rho_0}$ versus $\frac{T}{D}$ for $0.75 \leq n \leq 0.85$, where $\rho_0 = \frac{1}{\sigma_0}$. These resistivity curves have both the same shape and the same scale as those found through DMFT (see Fig. (1a) of Ref. [42]). We find a Fermi liquid regime $[\frac{\rho_{dc}}{\rho_0} \propto (\frac{T}{D})^2]$ for $0 < T < T_{FL}$, where $T_{FL} = (cD) \times Z(T=0)$, and $c \approx 0.05$. Furthermore, $\frac{\rho_{dc}}{\rho_0}$ is a function of $\frac{T}{DZ(T=0)}$ for $T \lesssim 2T_{FL}$ [Fig. 10(c)]. An important scale emphasized in DMFT studies [42,43] is the Brinkman-Rice scale ($T_{BR} = D\delta$), which is the renormalized bandwidth of the quasiparticles rather than the quasiparticle weight. Since $Z(T=0) \propto \delta^\alpha$, with $\alpha > 1$, the Fermi liquid scale is contained within the Brinkman-Rice scale, and is smaller than the latter by some power of δ . As T is increased above T_{FL} , the Fermi liquid regime is followed by a linear regime for $T_{FL} < T \lesssim 0.01D$. In Fig. 10(a), the Fermi liquid regime is tracked using the blue dashed parabola, while the linear regime is tracked using the magenta dashed line. Finally, this linear regime connects continuously to a second linear regime, existing for $T \gtrsim 0.07D$ [displayed in Fig. 10(b)].

We now analyze more closely the low-temperature regime ($T \lesssim 0.01D$). For this range of temperatures, the Sommerfeld

expansion can be applied to Eq. (44). To leading order $[-\partial f / \partial \omega = \delta(\omega)]$, and using Eq. (46), this gives

$$\rho_{DC} \sim \rho_0 \frac{-\text{Im} \Sigma(0, T)}{[1 - \{\mu - \text{Re} \Sigma(0, T)\}^2]^{3/2}}. \quad (47)$$

The constituent objects $-\text{Im} \Sigma(0, T)$ and $A(0, T)$ are plotted along with $Z(T)$ in the relevant temperature range in Fig. 11. We first examine $A(0, T) = \mu - \text{Re} \Sigma(0, T)$, displayed in Fig. 11(c). For $T_{FL} \lesssim T \lesssim 0.01D$, it is linear, as tracked by the dashed blue line. We also notice that $A^2(0, T) \ll 1$, and can therefore be neglected in Eq. (47). Equation (47) then implies that the resistivity is proportional to $[-\text{Im} \Sigma(0, T)]$ in this low-temperature range. Accordingly, in Fig. 11(a), we see that $[-\text{Im} \Sigma(0, T)]$ is quadratic for $T \lesssim T_{FL}$ (tracked by the blue dashed parabola) and linear for $T_{FL} \lesssim T \lesssim 0.01D$ (tracked by the magenta dashed line). Finally, in Fig. 11(b), we see that $Z(T)$ is approximately constant for $T \lesssim T_{FL}$, and grows linearly for $T_{FL} \lesssim T \lesssim 0.01D$, with a slope on the order of the bandwidth (tracked by the magenta dashed line). The blue dashed curve tracks the functional form discussed below, which approximates $Z(T)$ very well for $T \gtrsim T_{FL}$. As emphasized in [43], the temperature dependence of $[-\text{Im} \Sigma(0, T)]$ and $Z(T)$ lead to a quasiparticle scattering rate, defined as $[-\text{Im} \Sigma(0, T)] \times Z(T)$, which is quadratic well above T_{FL} .

In Fig. 12, we plot the temperature dependence of these objects in a broader temperature range. In Fig. 12(c), the blue dashed line indicates the presence of a second linear regime in $A(T)$ (with a slope slightly smaller than the first), meeting the latter at a kink at $T \approx 0.01D$. Figure 12(a) shows that for

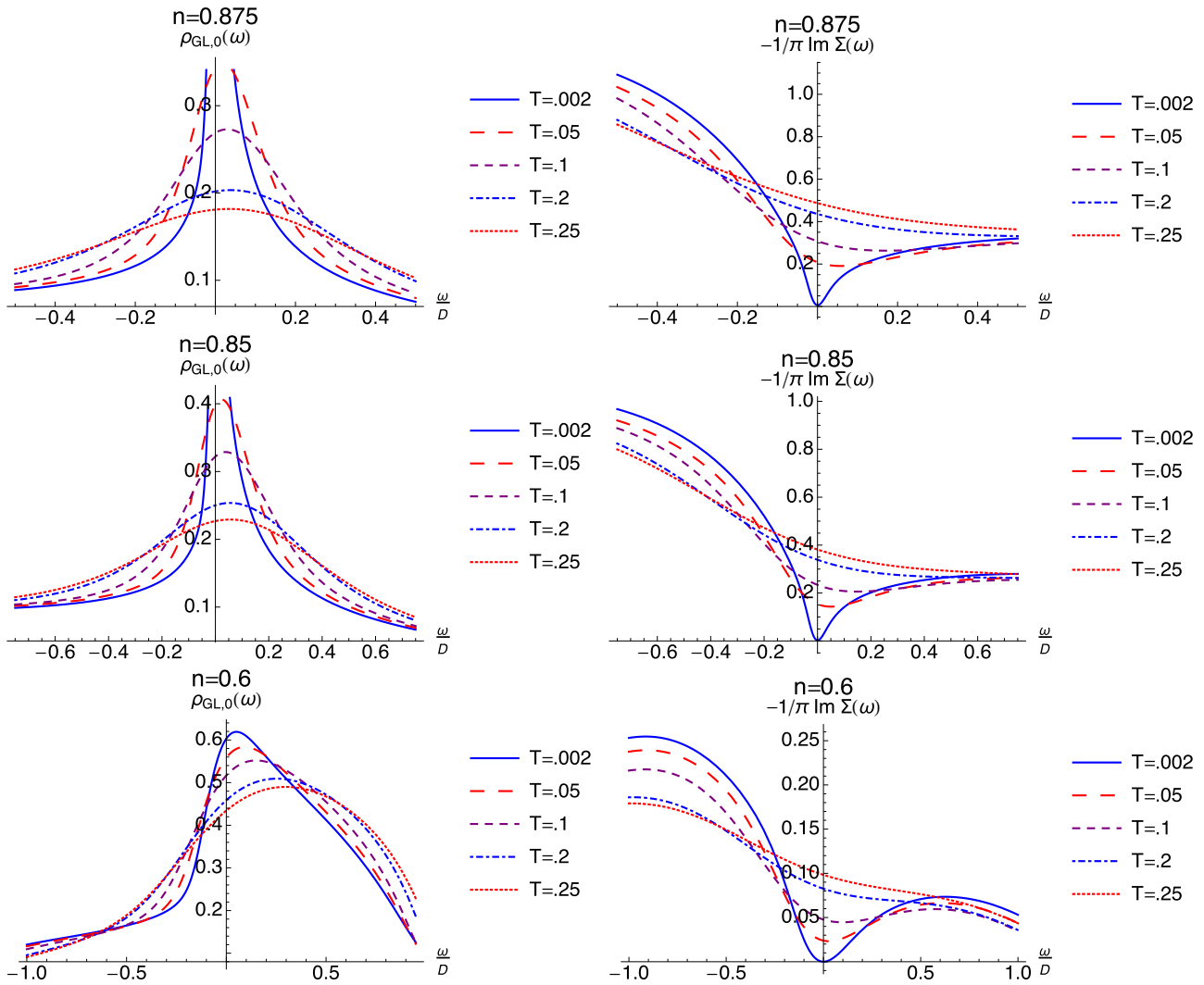


FIG. 9. The temperature variation with the frequency ω/D , of the spectral function $\rho_{GL,0}$ on the left and the Dyson self-energy $-\frac{1}{\pi} \text{Im} \Sigma$ on the right, at density $n = 0.875$ (top), $n = 0.85$ (middle), and at $n = 0.6$ (bottom). With increasing T we note the rapid broadening and shifting of $\rho_{GL,0}$. Here, $-\frac{1}{\pi} \text{Im} \Sigma$ displays a rapid destruction of the coherent Fermi liquid behavior observed at the lowest T , by the filling up of the minimum at $\omega = 0$. Comparing the top two sets shows that at the lowest hole density, a small change in T has a large effect, due to the low effective Fermi temperature. We also observe here, as well as in Fig. 8, that $-\frac{1}{\pi} \text{Im} \Sigma$ has a strong asymmetric correction to the quadratic ω dependence of the standard Fermi liquid, as highlighted in the bottom left panel of Fig. 7. This is in accord with one of the basic analytical predictions of the ECFL theory, and also is found in the DMFT results.

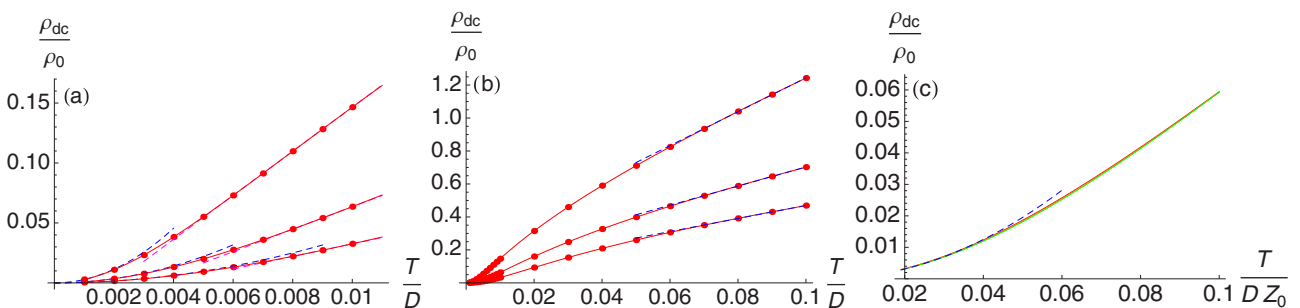


FIG. 10. (a), (b) $\frac{\rho_{dc}}{\rho_0}$ vs $\frac{T}{D}$ for $n = 0.75, 0.8, 0.85$ from bottom to top. In (a), the blue dashed parabola tracks the FL regime $0 < T < T_{FL}$ where $\frac{\rho_{dc}}{\rho_0} \propto (\frac{T}{D})^2$. The magenta dashed line tracks the first linear regime $T_{FL} < T \lesssim 0.01D$. In (b), the blue dashed line tracks the second linear regime $T \gtrsim 0.07D$. (c) $\frac{\rho_{dc}}{\rho_0}$ vs $\frac{T}{DZ(T=0)}$ for $n = 0.75, 0.8, 0.85$ (red, orange, green). The blue dashed parabola tracks the Fermi liquid regime, demonstrating that $T_{FL} = (cD) \times Z(T=0)$, with $c \approx 0.05$, and that $\frac{\rho_{dc}}{\rho_0}$ is a function of $\frac{T}{DZ(T=0)}$ for $T \gtrsim 2T_{FL}$.

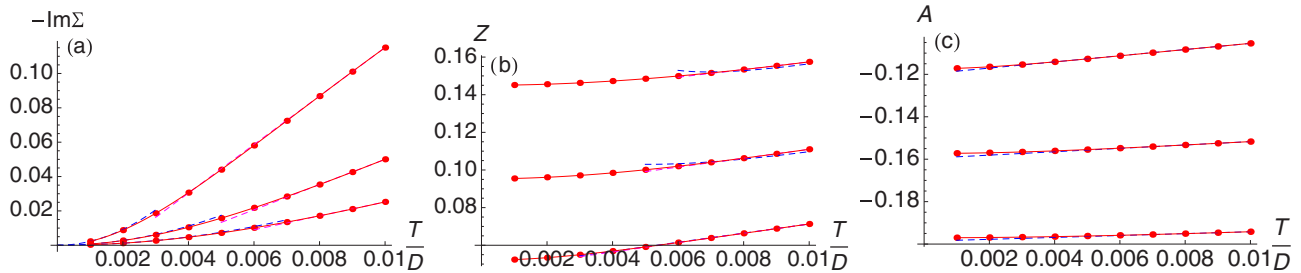


FIG. 11. (a) $[-\text{Im}\Sigma(0,T)]$ vs $\frac{T}{D}$ for $n = 0.75, 0.8, 0.85$ from bottom to top. $[-\text{Im}\Sigma(0,T)]$ is quadratic for $T \lesssim T_{\text{FL}}$ (tracked by the blue dashed parabola) and linear for $T_{\text{FL}} \lesssim T \lesssim 0.01D$ (tracked by the magenta dashed line). (b) $Z(T)$ vs $\frac{T}{D}$ for $n = 0.75, 0.8, 0.85$ from top to bottom. $Z(T)$ is approximately constant for $T \lesssim T_{\text{FL}}$, and grows linearly for $T_{\text{FL}} \lesssim T \lesssim 0.01D$, with a slope on the order of the bandwidth (tracked by the magenta dashed line). The blue dashed curve is the fit to the functional form $Z(T) = \sqrt{\frac{1+aT+bT^2}{c+dT}}$ using a broader range of temperatures than the one shown here [Fig. 12(b)]. This form works well for $T \gtrsim T_{\text{FL}}$. (c) $A(0,T) = \mu(T) - \text{Re} \Sigma(0,T)$ vs $\frac{T}{D}$ for $n = 0.75, 0.8, 0.85$ from bottom to top. For $T_{\text{FL}} \lesssim T \lesssim 0.01D$, it is linear, as tracked by the dashed blue line.

$T > 0.01D$, $[-\text{Im}\Sigma(0,T)]$ continues to grow, until it finally begins to saturate at higher temperatures. Finally, in Fig. 12(b), we fit $Z(T)$ to the functional form $Z(T) = \sqrt{\frac{1+aT+bT^2}{c+dT}}$, tracked by the blue dashed curve. This form works well for $T \gtrsim T_{\text{FL}}$. For $T \lesssim 0.01D$, it reproduces the behavior shown in Fig. 11(b), while for $T \gtrsim 0.01D$, it is consistent with the behavior $Z(T) \propto \sqrt{T}$. Therefore, $Z^2(T)$ is linear in T over a very wide temperature range starting with $T \approx 0.01D$.

VII. CONCLUSIONS

In this work, we have presented an analytical calculation of properties of the t - J model in infinite dimensions, and shown that it provides a quantitative description of variables known from exact numerical work in [42,43]. The results include the quasiparticle weight, the self-energies, and spectral functions with particle-hole asymmetry that have been argued to be characteristic of very strong correlation [6,8]. Finally, we also give a good account of the temperature variation of resistivity. Results with the present technique at high T are less reliable and are not presented. In the low- to intermediate- T results reported here, we reproduce the main features of the exact DMFT calculations, including a narrow regime with quadratic T dependence followed by two distinct linear T -dependent regimes. We are further able to identify the origin of these regimes in terms of the parameters of the theory.

The t - J model studied here contains two essential ingredients of strong correlations: the physics of Gutzwiller projection to the subspace of single occupancy, and the physics of the superexchange. The first is captured in the present scheme, while the second is lost since we limit the study to infinite dimension for the purpose of benchmarking against known exact results. The scheme by itself has no intrinsic limitations to the case studied, and is generalizable to finite dimensions as well as finite superexchange. Thus, it may be expected to yield interesting results in lower dimensions, including transitions between different broken-symmetry states. Such calculations are currently underway.

In this work, we have discussed the characteristics of the resulting ECFL state. The state reported here is Fermi liquid like, but only so at a surprisingly low temperature. Upon minimal warming, this state devolves into one exhibiting linear resistivity. Our calculation yields a reduction of the effective Fermi temperature, due to extreme correlations, that far exceeds the expectations [58] based on a simple estimate $T_F^{\text{eff}} \sim \delta T_F$.

Within the terms of its limitations of $d \rightarrow \infty$ and $J = 0$, this work provides useful insights. At the density $n \sim 0.85$ relevant for cuprate superconductors, we obtain a state displaying linear resistivity for T beyond ~ 45 K as seen in Fig. 1. A similar onset of linearity occurs at a slightly higher T within DMFT, the difference is due to our Z (from Fig. 6) being about half of the exact value. If we imagine that the effects of reduced dimensionality and nonzero J can stabilize

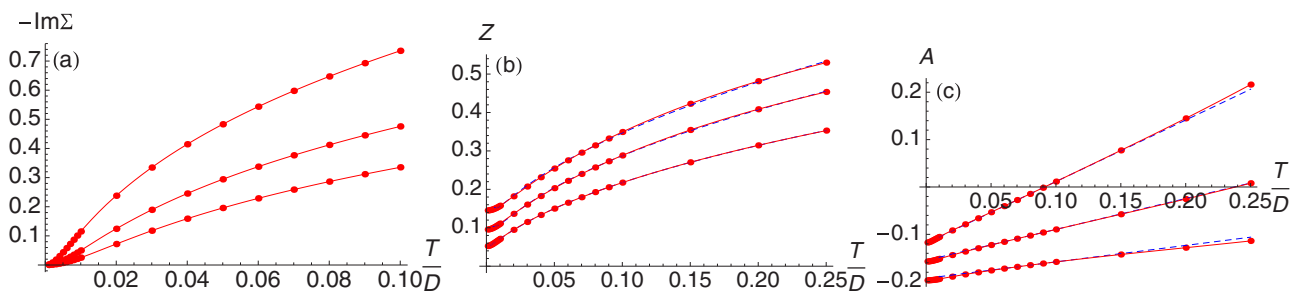


FIG. 12. Same plots as in Fig. 11 over a broader range of temperatures. (a) $[-\text{Im}\Sigma(0,T)]$ continues to grow as T is increased beyond $0.01D$, until it finally begins to saturate at higher temperatures. (b) The blue dashed curve is the fit to the functional form $Z(T) = \sqrt{\frac{1+aT+bT^2}{c+dT}}$, which works well for $T \gtrsim T_{\text{FL}}$. For $T \gtrsim 0.01D$, $Z(T) \propto \sqrt{T}$. (c) The blue dashed line tracks the second linear regime in $A(T)$ (with a slope slightly smaller than the first) for $T \gtrsim 0.01D$.

this smaller onset scale, then the possibility of observing the asymptotic T^2 resistivity of a Fermi liquid would become remote. Thus, the quadratic behavior, so essential for making a *formal distinction* between Fermi liquids and the elusive non-Fermi liquids [59], could be rendered unobservable in practice as well as divested of any essential difference.

ACKNOWLEDGMENTS

We thank A. Georges for useful discussions about resistivity in DMFT. The work at UCSC was supported by the U. S. Department of Energy (DOE), Office of Science, Basic Energy Sciences (BES) under Award No. DE-FG02-06ER46319.

-
- [1] P. W. Anderson, *Science* **235**, 1196 (1987).
- [2] B. S. Shastry, *Phys. Rev. Lett.* **107**, 056403 (2011); **108**, 029702 (2012).
- [3] B. S. Shastry, *Ann. Phys. (NY)* **343**, 164 (2014).
- [4] F. J. Dyson, *Phys. Rev.* **102**, 1230 (1956); S. V. Maleev, *Zh. Eksp. Teor. Fiz.* **33**, 1010 (1957) [*Sov. Phys.-JETP* **6**, 776 (1958)]; A. B. Harris, D. Kumar, B. I. Halperin, and P. C. Hohenberg, *Phys. Rev. B* **3**, 961 (1971).
- [5] B. S. Shastry, E. Perepelitsky, and A. C. Hewson, *Phys. Rev. B* **88**, 205108 (2013).
- [6] R. Žitko, D. Hansen, E. Perepelitsky, J. Mravlje, A. Georges, and B. S. Shastry, *Phys. Rev. B* **88**, 235132 (2013).
- [7] G.-H. Gweon, B. S. Shastry, and G. D. Gu, *Phys. Rev. Lett.* **107**, 056404 (2011).
- [8] B. S. Shastry, *Phys. Rev. Lett.* **109**, 067004 (2012).
- [9] K. G. Wilson, *Rev. Mod. Phys.* **47**, 773 (1975).
- [10] H. R. Krishna-murthy, J. W. Wilkins, and K. G. Wilson, *Phys. Rev. B* **21**, 1044 (1980).
- [11] T. A. Costi, J. Kroha, and P. Wölfle, *Phys. Rev. B* **53**, 1850 (1996).
- [12] T. A. Costi and A. C. Hewson, *J. Phys. C* **5**, L361 (1993).
- [13] A. Georges, G. Kotliar, W. Krauth, and M. J. Rozenberg, *Rev. Mod. Phys.* **68**, 13 (1996).
- [14] W. Metzner and D. Vollhardt, *Phys. Rev. Lett.* **62**, 324 (1989).
- [15] Y. Kuramoto and T. Watanabe, *Physica B (Amsterdam)* **148**, 246 (1987); O. Sakai and Y. Kuramoto, *Solid State Commun.* **89**, 307 (1994).
- [16] D. Nicoletti, O. Limaj, P. Calvani, G. Rohringer, A. Toschi, G. Sangiovanni, M. Capone, K. Held, S. Ono, Yoichi Ando, and S. Lupi, *Phys. Rev. Lett.* **105**, 077002 (2010).
- [17] G. R. Boyd, V. Zlatic, and J. K. Freericks, *Phys. Rev. B* **91**, 075118 (2015).
- [18] R. Bulla, *Phys. Rev. Lett.* **83**, 136 (1999).
- [19] R. Chitra and G. Kotliar, *Phys. Rev. Lett.* **83**, 2386 (1999).
- [20] Marcelo J. Rozenberg, R. Chitra, and Gabriel Kotliar, *Phys. Rev. Lett.* **83**, 3498 (1999).
- [21] K. Held and D. Vollhardt, *Phys. Rev. Lett.* **84**, 5168 (2000).
- [22] Massimo Capone, Michele Fabrizio, Claudio Castellani, and Erio Tosatti, *Phys. Rev. Lett.* **93**, 047001 (2004).
- [23] D. J. Garcia, Karen Hallberg, and Marcelo J. Rozenberg, *Phys. Rev. Lett.* **93**, 246403 (2004).
- [24] Krzysztof Byczuk, Walter Hofstetter, and Dieter Vollhardt, *Phys. Rev. Lett.* **94**, 056404 (2005).
- [25] M. Keller, W. Metzner, and U. Schollwock, *Phys. Rev. Lett.* **86**, 4612 (2001).
- [26] A. I. Lichtenstein, M. I. Katsnelson, and G. Kotliar, *Phys. Rev. Lett.* **87**, 067205 (2001).
- [27] Gabriel Kotliar, Sergej Y. Savrasov, Gunnar Pálsson, and Giulio Biroli, *Phys. Rev. Lett.* **87**, 186401 (2001).
- [28] A. Chattopadhyay, S. Das Sarma, and A. J. Millis, *Phys. Rev. Lett.* **87**, 227202 (2001).
- [29] Antoine Georges, Rahul Siddharthan, and Serge Florens, *Phys. Rev. Lett.* **87**, 277203 (2001).
- [30] B. Kyung and A.-M. S. Tremblay, *Phys. Rev. Lett.* **97**, 046402 (2006).
- [31] Junya Otsuki, Hiroaki Kusunose, and Yoshio Kuramoto, *Phys. Rev. Lett.* **102**, 017202 (2009).
- [32] Michael Potthoff, *Phys. Rev. B* **64**, 165114 (2001).
- [33] K.-S. Chen, Z. Y. Meng, S.-X. Yang, T. Pruschke, J. Moreno, and M. Jarrell, *Phys. Rev. B* **88**, 245110 (2013).
- [34] M. H. Hettler, M. Mukherjee, M. Jarrell, and H. R. Krishnamurthy, *Phys. Rev. B* **61**, 12739 (2000).
- [35] M. Jarrell and H. R. Krishnamurthy, *Phys. Rev. B* **63**, 125102 (2001).
- [36] Luigi Amico and Vittorio Penna, *Phys. Rev. Lett.* **80**, 2189 (1998).
- [37] Marcus Fleck, Alexander I. Liechtenstein, Andrzej M. Oleś, Lars Hedin, and Vladimir I. Anisimov, *Phys. Rev. Lett.* **80**, 2393 (1998).
- [38] Gunnar Pálsson and Gabriel Kotliar, *Phys. Rev. Lett.* **80**, 4775 (1998).
- [39] A. J. Millis, Jun Hu, and S. Das Sarma, *Phys. Rev. Lett.* **82**, 2354 (1999).
- [40] For example, in [6] we comment on the insufficient height of the peak in the imaginary part of self-energy on the occupied side, and the absent “nipple” in the ECFL spectrum. We also note that for a few cases, the high-energy $\omega \gg ZD$ (actually for $\omega > 1.5D$) *unoccupied states* show unphysical negative weights. Their occasional appearance seems difficult to avoid completely at the current preliminary stage of development in this unconventional theory. In the authors’ view, a mitigating factor is that such errors arise at very high excitation energies, a regime that is not easily probed, at least within ARPES. This regime is also irrelevant for the number sum rule, where only occupied states are counted. We should therefore be careful in relying on the results for high-energy unoccupied states beyond say $\omega \geq D$.
- [41] A. Khurana, *Phys. Rev. Lett.* **64**, 1990 (1990).
- [42] X. Deng, J. Mravlje, R. Žitko, M. Ferrero, G. Kotliar, and A. Georges, *Phys. Rev. Lett.* **110**, 086401 (2013).
- [43] W. Xu, K. Haule, and G. Kotliar, *Phys. Rev. Lett.* **111**, 036401 (2013).
- [44] The term *caparison*, defined in www.merriam-webster.com/dictionary as *rich clothing* or *adornment*, is used to stress the idea that the physical Green’s function \mathcal{G} acquires a second dressing (renormalization) on top of the

standard dressing provided the Dyson-type self-energy of the auxiliary Green's function \mathbf{g} , namely, by Φ .

- [45] E. Perepelitsky and B. S. Shastry, *Ann. Phys. (NY)* **338**, 283 (2013).
- [46] E. Perepelitsky and B. S. Shastry, *Ann. Phys. (NY)* **357**, 1 (2015).
- [47] B. S. Shastry, *Phys. Rev. B* **87**, 125124 (2013).
- [48] These equations can be found in [46] [Eqs. (56)–(61)] by setting the exchange $J \rightarrow 0$. In particular, Eq. (65a) gives the quoted $\Psi_{[1]}$, Eq. (66a) gives the quoted $\chi_{[0]}$, and Eqs. (66b) and (67a) give the quoted $\chi_{[1]}$. We stress that in this version, the sum rule for γ is used exactly and hence we retain only the first term (64a) and abandon the higher-order λ expansion terms [Eqs. (64b)–(64d), etc.].
- [49] D. Hansen and B. S. Shastry, *Phys. Rev. B* **87**, 245101 (2013).
- [50] N. Prokof'ev and B. Svistunov, *Phys. Rev. Lett.* **99**, 250201 (2007).
- [51] E. Kozik, K. Van Houcke, E. Gull, L. Pollet, N. Prokof'ev, B. Svistunov and M. Troyer, *Europhys. Lett.* **90**, 10004 (2010).
- [52] N. V. Prokofiev, B. V. Svistunov, and I. S. Tupitsyn, *Phys. Lett. A* **238**, 253 (1993).
- [53] W.-C. Lee and P. W. Phillips, *Phys. Rev. B* **84**, 115101 (2011).
- [54] The other half is clearly in the occupied region $\omega < 0$.
- [55] M. R. Peterson and B. S. Shastry, *Phys. Rev. B* **82**, 195105 (2010); B. S. Shastry, *Rep. Prog. Phys.* **72**, 016501 (2009).
- [56] W. F. Brinkman and T. M. Rice, *Phys. Rev. B* **2**, 4302 (1970).
- [57] The value $\Phi(0)$ can be calculated as

$$\Phi(0) = \frac{D^3}{2\pi(a_0 d \hbar^2)} \frac{\varepsilon_F}{(D^2 - \varepsilon_F^2)^{3/2}},$$

and yields an estimate of the IRM conductivity scale

$$\sigma_0 = \left(\frac{e^2}{h} \frac{1}{a_0 d} \right) \frac{D^2 \varepsilon_F}{(D^2 - \varepsilon_F^2)^{3/2}}.$$

The proportionality to inverse dimension is expected since the current flows in one of d directions.

- [58] Using $C \equiv k_B \frac{T}{T_F}$ for a band of noninteracting electrons, where C is the specific heat, we find that $T_F = \frac{3}{4\pi} \frac{D}{k_B}$. With the half-bandwidth $D \sim 12000$ K (1 eV) a naive estimate using $n = 0.85$ and a crude formula $T_F^{\text{eff}} = \delta T_F$ would yield $T_F^{\text{eff}} \sim 430$ K. In DMFT [42], this scale is reduced to 90 K, while in the present theory, it is reduced even further down to 30 K.
- [59] R. B. Laughlin, *Phys. Rev. Lett.* **112**, 017004 (2014).